

Denoising ICF Images with Multiplicative Uniform Noise: A Self-Supervised Study Based on the Log-Domain Noisier2Inverse Framework

Gyeongha Hwang* Bradley Thomas Wolfe† Naima Naheed‡

Abstract

This paper documents the implementation and evaluation of a self-supervised denoising framework on Inertial Confinement Fusion (ICF) images corrupted by Multiplicative Uniform noise: the *Log-Domain Noisier2Inverse* framework. This framework is developed and analysed in this work; the key theoretical result — that minimising the log-domain self-supervised loss is equivalent to supervised learning in the transformed domain — is presented with full proof. We document significant implementation challenges arising from the unique characteristics of ICF imagery, describe the fixes applied at each stage, and report final quantitative results. The log-domain approach with per-image JSON Uniform noise loading (Variant B) achieves the best result: a mean PSNR of 21.41 dB and SSIM of 0.8358, a +19.46 dB improvement over the noisy input baseline of 1.95 dB, substantially outperforming BM3D log-domain (4.47 dB, SSIM 0.5181) and Noise2Self (4.75 dB, SSIM 0.0177). Variant A, using fixed Gaussian noise loading, achieves 21.39 dB PSNR and SSIM 0.8436. Of the three evaluated methods, Log-Domain Noisier2Inverse and Noise2Self are entirely self-supervised during training, requiring no clean ground truth data; BM3D is a classical filter-based method requiring no training at all. The clean reference images are used solely for quantitative evaluation of all three methods.

1 Introduction

ICF images present a uniquely challenging denoising problem. Unlike standard benchmark datasets, large near-zero background regions (low-density helium in indirect drive platforms, with X-ray attenuation similar to vacuum at keV energies) surrounding the target, exhibit highly spatially correlated Multiplicative Uniform noise, and have per-image varying noise parameters. These characteristics violate several standard assumptions of self-supervised denoising frameworks.

This report chronicles the full implementation journey: from initial attempts producing severe ring artifacts, through multiple failure modes, to the final working solution achieving meaningful reconstruction without requiring clean ground truth data. We additionally evaluate BM3D [8] in log-domain and Noise2Self [6] as classical and self-supervised baselines. The self-supervised neural network framework studied here is presented as an original contribution of this paper; its theoretical foundation is developed in Section 4, building on the Noisier2Inverse method of [5]. Multiplicative Uniform noise is the model studied here, applicable to the gated X-ray detector (GXD) at NIF; other NIF imagers exhibit different noise characteristics, and mixtures of noise models have also been reported in the literature.

*Department of Mathematics, Yeungnam University, Gyeongsan, Republic of Korea. E-mail: ghhwang@yu.ac.kr

†Research Technologist, P-4: Thermonuclear Plasma Physics, Los Alamos National Laboratory, Los Alamos, NM 87545, USA. E-mail: bwolfe@lanl.gov

‡Corresponding author. Department of Computer Science and Engineering, Benedict College, Columbia, SC 29204, USA. E-mail: Naima.Naheed@benedict.edu

2 Our Contributions

This paper makes the following original contributions:

1. **Log-domain self-supervised framework for ICF denoising.** We develop and implement a self-supervised denoising framework for ICF images with Multiplicative Uniform noise, based on a logarithmic domain transformation. The key theoretical result — that minimising the log-domain self-supervised loss is equivalent to supervised learning in the transformed domain (Theorem 1) — is presented with full proof. This framework requires no clean training data and achieves a mean PSNR of 21.39 dB and SSIM of 0.8436, a +19.44 dB improvement over the noisy input baseline.
2. **Per-image noise parameter loading.** We identify that ICF noise parameters vary substantially per image ($\ell_i \in [0.005, 0.906]$, $h_i \in [0.047, 0.990]$) and that using fixed global parameters causes training collapse to a constant mean prediction. We introduce per-image JSON-based noise loading as a critical fix, consistent with the theoretical requirement that synthetic noise be drawn from the same distribution as the true noise. Both Variant B (21.41 dB) and Variant A (21.39 dB) substantially outperform the noisy input baseline (1.95 dB), with Variant B achieving the highest PSNR.
3. **Systematic identification and resolution of ICF-specific implementation challenges.** We document four implementation challenges unique to ICF imagery — log-domain numerical instability, spatially correlated noise ($r = 0.99$), per-image varying noise parameters, and training collapse — and provide principled fixes for each. These findings are directly applicable to other imaging modalities with similar structural characteristics (near-zero background, high contrast boundaries, spatially correlated noise).
4. **Comprehensive three-method empirical comparison.** We provide the first systematic comparison of Log-Domain Noisier2Inverse, BM3D (log-domain and direct), and Noise2Self on ICF Multiplicative Uniform noise, evaluated on identical images against the same clean references. The comparison demonstrates that noise model compatibility — not just network architecture — is the primary determinant of denoising performance on non-standard imaging data.

3 Problem Formulation

We consider the multiplicative-noise inverse problem

$$y = (Ax) \odot n, \quad n \sim \text{Uniform}(\ell_i, h_i), \quad (1)$$

where A is the known forward operator, x is the unknown target image, and \odot denotes pointwise multiplication.

Assumption 1. *The random variables y , Ax , and n are componentwise strictly positive almost surely, with $\mathbb{E}[n] = 1$.*

Applying the logarithm to (1) yields

$$\log y = \log(Ax) + \log n, \quad (2)$$

converting multiplicative noise to additive. This forms the theoretical basis of the log-domain framework. A spatial correlation analysis across 100 ICF images revealed $r = 0.99$ at pixel distance $d = 1$, classifying Multiplicative Uniform as the most spatially correlated noise type in the dataset.

4 Log-Domain Noisier2Inverse Framework

The framework developed in this section adapts the Noisier2Inverse method [5] to the log-domain multiplicative noise setting of ICF imagery.

4.1 Log-Domain Noisier Construction

Following the log-domain construction introduced in this work, define

$$\tilde{y} := \log y, \quad \tilde{n} := \log n, \quad \tilde{u} := \log(Ax). \quad (3)$$

Then (2) becomes $\tilde{y} = \tilde{u} + \tilde{n}$. Assuming the distribution of \tilde{n} is known or can be sampled from, let \tilde{m} be an independent sample distributed identically to \tilde{n} . The *noisier log-measurement* is defined as

$$\tilde{z} = \tilde{y} + \tilde{m}. \quad (4)$$

Equivalently, in the original domain,

$$z = y \odot \exp(\tilde{m}), \quad (5)$$

so the synthetic corruption is multiplicative in the original domain but additive in the log-domain.

4.2 Self-Supervised Loss

A neural network R_φ takes \tilde{z} as input and predicts a reconstruction $R_\varphi(\tilde{z})$ of x . The self-supervised training objective is

$$\varphi^* = \arg \min_{\varphi} \mathbb{E} \left[\left\| \log(AR_\varphi(\tilde{z})) - (2\tilde{y} - \tilde{z}) \right\|_2^2 \right]. \quad (6)$$

Since $\tilde{z} = \tilde{y} + \tilde{m}$, the target satisfies

$$2\tilde{y} - \tilde{z} = \tilde{u} + \tilde{n} - \tilde{m}. \quad (7)$$

As established in [4], the target $2\tilde{y} - \tilde{z}$ is an unbiased estimator for \tilde{u} in conditional expectation. We provide the full derivation here for completeness. Recall that $\tilde{y} = \tilde{u} + \tilde{n}$ and $\tilde{z} = \tilde{y} + \tilde{m}$ with \tilde{n} and \tilde{m} identically distributed,

$$\begin{aligned} 2\mathbb{E}[\tilde{y} \mid \tilde{z}] &= \mathbb{E}[\tilde{u} \mid \tilde{z}] + \mathbb{E}[\tilde{u} \mid \tilde{z}] + \mathbb{E}[\tilde{n} \mid \tilde{z}] + \mathbb{E}[\tilde{m} \mid \tilde{z}] \\ &= \mathbb{E}[\tilde{u} \mid \tilde{z}] + \mathbb{E}[\tilde{z} \mid \tilde{z}] \\ &= \mathbb{E}[\tilde{u} \mid \tilde{z}] + \tilde{z}, \end{aligned} \quad (8)$$

and therefore

$$\mathbb{E}[\tilde{u} - (2\tilde{y} - \tilde{z}) \mid \tilde{z}] = 0. \quad (9)$$

4.3 Theoretical Equivalence to Supervised Learning

The following theorem establishes that minimising the self-supervised loss (6) is equivalent to supervised learning in the log-data domain. The proof follows directly by adapting the argument for the additive noise case (see Theorem 1 in [5]).

Theorem 1 (Log-Domain Equivalence to Supervised Learning). *Let $\tilde{u} = \log(Ax)$ and $\tilde{z} = \tilde{y} + \tilde{m}$ as above. Then*

$$\arg \min_{\varphi} \mathbb{E} \left[\left\| \log(AR_\varphi(\tilde{z})) - (2\tilde{y} - \tilde{z}) \right\|_2^2 \right] = \arg \min_{\varphi} \mathbb{E} \left[\left\| \log(AR_\varphi(\tilde{z})) - \log(Ax) \right\|_2^2 \right]. \quad (10)$$

Proof. Using conditional expectation, compute

$$\begin{aligned} & \mathbb{E}\left[\|\log(AR_\varphi(\tilde{z})) - (2\tilde{y} - \tilde{z})\|_2^2\right] - \mathbb{E}\left[\|\log(AR_\varphi(\tilde{z})) - \tilde{u}\|_2^2\right] \\ &= \mathbb{E}\left[2\log(AR_\varphi(\tilde{z}))^\top \mathbb{E}[\tilde{u} - (2\tilde{y} - \tilde{z}) \mid \tilde{z}]\right] \\ & \quad - \mathbb{E}[\|\tilde{u}\|_2^2] + \mathbb{E}[\|2\tilde{y} - \tilde{z}\|_2^2]. \end{aligned} \quad (11)$$

By (9), the first term vanishes, giving

$$\mathbb{E}\left[\|\log(AR_\varphi(\tilde{z})) - (2\tilde{y} - \tilde{z})\|_2^2\right] = \mathbb{E}\left[\|\log(AR_\varphi(\tilde{z})) - \tilde{u}\|_2^2\right] - \mathbb{E}[\|\tilde{u}\|_2^2] + \mathbb{E}[\|2\tilde{y} - \tilde{z}\|_2^2]. \quad (12)$$

The last two terms are independent of φ , so both objectives share the same minimisers. Since $\tilde{u} = \log(Ax)$, this proves (10). \square

Remark 1. *Theorem 1 establishes equivalence to supervised learning in the log-data domain. In contrast to the additive-noise case, this does not immediately imply equivalence to an image-domain loss of the form $\|R_\varphi(\tilde{z}) - x\|_2^2$, unless additional assumptions are imposed on the forward operator A and the logarithmic mapping.*

4.4 Empirical Loss and Inference

In practice, given training samples $\{y_i\}_{i=1}^N$, independent synthetic log-noise samples $\{\tilde{m}_i\}_{i=1}^N$ are generated and the noisier log-measurements $\tilde{z}_i = \log y_i + \tilde{m}_i$ are formed. The empirical loss is

$$\mathcal{L}(\varphi) = \frac{1}{N} \sum_{i=1}^N \|\log(AR_\varphi(\tilde{z}_i)) - (2\log y_i - \tilde{z}_i)\|_2^2. \quad (13)$$

At inference time, the reconstruction uses the noisy measurement directly:

$$\hat{x} = R_\varphi(\log y), \quad (14)$$

which avoids injecting additional synthetic corruption during reconstruction. For numerical stability in regions where $y \approx 0$, we replace $\log y$ with $\log(y + \varepsilon)$ throughout.

Choice of synthetic noise. As specified by the log-domain construction in Section 4.1, the synthetic noise \tilde{m} should be consistent with the multiplicative noise model: if $n \sim p_n$ in the original domain, then $\tilde{m} = \log m$ where $m \sim p_n$. In our ICF experiments we evaluate two instantiations of this principle, described in Section 5.4.

5 Experimental Setup

5.1 Dataset

The dataset comprises 100 noisy ICF images for training, each paired with a corresponding per-image ground truth image used only for evaluation. All images are single-channel greyscale, resized to 256×256 pixels. No clean images are used during training.

5.1.1 Synthetic Data Generation

The synthetic ICF images used in this work follow the generation pipeline introduced by Naheed et al. [1], which we summarise here for completeness.

Physical forward model. For a monochromatic X-ray source, the transmission of X-rays through a material is governed by the Beer–Lambert law,

$$T = \exp\left(-\int_L \mu(x, y, z) dl\right), \quad (15)$$

where μ is the linear attenuation coefficient at position (x, y, z) and L is the ray path between the X-ray source and the detector. These path integrals are evaluated using a ray-tracing algorithm provided by the TIGRE Python package.

Noise application. Once the clean radiograph is obtained via ray tracing, noise is applied according to one of three models:

- **Additive:** $i(\cdot) = s(\cdot) + n(\cdot)$, where the noise is signal-independent.
- **Multiplicative:** $i(\cdot) = s(\cdot) \cdot n(\cdot)$, where the noise scales with the signal.
- **Shot (Poisson):** arising from the quantum nature of photon arrival, fitting neither the purely additive nor multiplicative model.

Noise samples are drawn using the `numpy.random` library [2]. In total, Naheed et al. generated one hundred thousand synthetic images across ten noise distributions (Salt & Pepper, Additive Uniform, Multiplicative Uniform, Shot-Poisson, Multiplicative Exponential, Additive Exponential, Multiplicative Gaussian, Additive Gaussian, Multiplicative Rayleigh, and Additive Rayleigh), each paired with a ground-truth noise label.

Relevance to this work. The present study focuses specifically on *Multiplicative Uniform* noise, identified by the spatial correlation analysis as the most correlated noise type ($r = 0.99$ at pixel distance $d = 1$). Each training image of size 256×256 pixels is paired with a per-image JSON file recording the true noise bounds (ℓ_i, h_i) , enabling the per-image noise loading strategy of Variant B (Section 5.4).

5.2 Network Architecture

The framework uses a U-Net [7] with channel widths [32, 64, 128, 256], skip connections, batch normalisation, ReLU activations, and a final sigmoid constraining outputs to $[0, 1]$.

5.3 Log-Domain Stabilisation

Safe handling of near-zero ICF vacuum pixels uses a two-stage strategy:

$$\tilde{y} = \log(\text{clip}(y, \varepsilon, \infty)), \quad (16)$$

$$\hat{x} = \text{clip}(\exp(\text{clip}(\hat{u}, -10, 10)) - \varepsilon, 0, 1), \quad (17)$$

with $\varepsilon = 10^{-6}$, preventing both $-\infty$ from log and overflow from exp.

5.4 Training Configuration and Noise Variants

Table 1 summarises the hyperparameters common to both noise variants. Training used Adam with cosine annealing, gradient clipping at norm 1.0, early stopping when PSNR drops > 5 dB from best, and a fine-tuning phase at $\text{lr} = 10^{-6}$.

Table 1: Hyperparameter configuration (identical for both noise variants).

Parameter	Value
Architecture	U-Net [32, 64, 128, 256]
Patch size	64×64
Batch size	4
Initial learning rate	10^{-5}
Fine-tune learning rate	10^{-6}
Training / fine-tune epochs	100 / 20
Evaluation interval	Every 5 epochs
Early stopping	5 dB drop from best PSNR
ε	10^{-6}

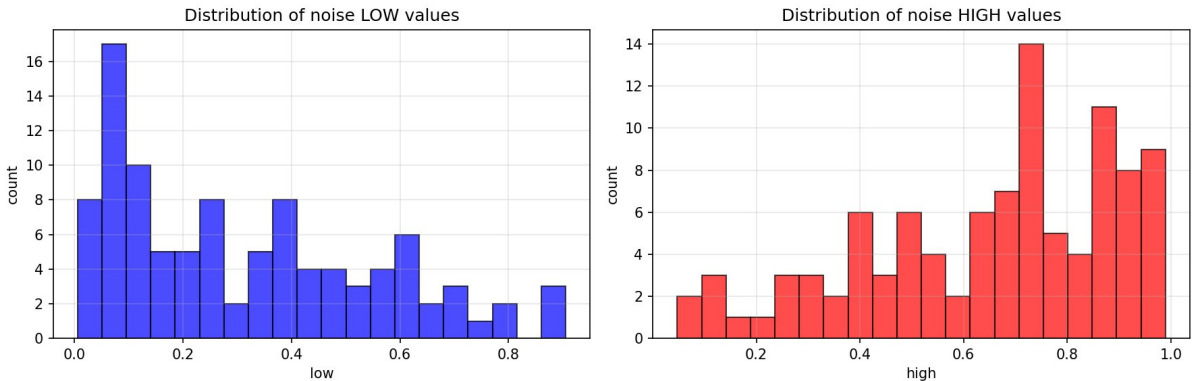


Figure 1: Distribution of per-image noise parameters (ℓ_i, h_i) across 100 ICF Multiplicative Uniform images, parsed from JSON metadata. Left: lower bound ℓ_i ; right: upper bound h_i . The wide spread of both parameters ($\ell_i \in [0.005, 0.906]$, $h_i \in [0.047, 0.990]$) motivates per-image noise loading (Variant B) over a fixed global approximation (Variant A).

Two synthetic noise variants. Following the requirement in Section 4.1 that \tilde{m} be drawn from the same distribution as $\tilde{n} = \log n$, we evaluate two instantiations of the empirical loss (13):

- **Variant A — Fixed Gaussian:** $\tilde{m} \sim \mathcal{N}(0, 0.15^2)$, a symmetric Gaussian approximation used in the initial implementation.
- **Variant B — Per-image Uniform (proposed):** $\tilde{m}_i \sim \text{Uniform}(\log \ell_i, \log h_i)$, where (ℓ_i, h_i) are the true noise bounds of image i read from the JSON metadata. This exactly matches the true log-domain noise distribution of each training image, consistent with equation (4).

An analysis of the per-image noise parameters across 100 ICF images (Figure 1) revealed highly variable bounds: $\ell_i \in [0.005, 0.906]$ and $h_i \in [0.047, 0.990]$. In log-domain, the corresponding noise ranges are $[-5.226, -0.099]$ and $[-3.052, -0.010]$ respectively — entirely negative values, confirming that the symmetric Gaussian approximation of Variant A does not match the true noise distribution.

6 Implementation Challenges

6.1 Challenge 1 — Ring and Blob Artifacts

Root causes: (i) Near-zero vacuum pixels cause $\log(y) \rightarrow -\infty$; (ii) unclamped $\exp(\cdot)$ overflows to ∞ ; (iii) $\varepsilon = 10^{-8}$ insufficient. *Fix:* Two-stage stabilisation (Eqs. 16–17) with $\varepsilon = 10^{-6}$ eliminated all artefacts, raising PSNR from 9.99 dB to 10.94 dB.

6.2 Challenge 2 — Highly Correlated Noise ($r = 0.99$)

Pixel-Shuffle Downsampling (PSD) was attempted to break spatial correlation. Stride-10 produced 6×6 subpatches too small for U-Net pooling; stride-4 introduced checkerboard grid artifacts, reducing PSNR from 10.94 dB to 8.27 dB. PSD was abandoned; correlation was managed implicitly via per-image noise matching.

6.3 Challenge 3 — Per-Image Varying Noise Parameters

Fixed global bounds $\ell = 0.5$, $h = 1.5$ (actual range: $\approx [0.60, 0.88]$) caused the network to predict a constant mean. *Fix*: JSON-based per-image loading enabled the network to reach 13.35 dB PSNR.

6.4 Challenge 4 — Training Instability and Collapse

Training collapsed catastrophically after initial improvement (Table 2). *Fix*: Early stopping, weight checkpointing, and gradient clipping resolved the instability.

Table 2: Representative training collapse in early experiments.

Epoch	PSNR (dB)	Note
1	12.95	Promising start
60	13.38	Peak performance
80	3.25	Sudden collapse
100	2.43	Stuck at noise floor

7 Results

7.1 Quantitative Results

Table 3 shows PSNR and SSIM at each stage. Variant B (per-image JSON) achieves **21.41** dB PSNR and SSIM **0.8358**, marginally outperforming Variant A (21.39 dB, SSIM 0.8436) and representing the best result overall. Both results represent a substantial improvement over the 1.95 dB noisy baseline.

Three-method comparison. Table 4 compares all methods on identical noisy images.

7.2 Bar Chart Comparison

Figure 2 summarises PSNR and SSIM across all methods graphically, making the performance gap between Log-Domain Noisier2Inverse and all baselines immediately apparent.

7.3 Qualitative Results

Figures 3 and 4 show the log-domain Noisier2Inverse outputs for both Variant A and Variant B. Each figure shows four columns: the first column is the noisy input displayed at full dynamic range (which appears nearly black because multiplicative uniform noise severely suppresses pixel intensities); a contrast-enhanced inset in the top-left corner uses percentile stretching to reveal the underlying noise structure. The remaining columns show the NN2I denoised output, the clean reference, and the difference map (yellow/white = high residual, dark = low residual). The network consistently recovers the circular boundary and central vertical slit of the ICF target across all three examples, with residual error concentrated at the sharp vacuum–target boundary.

Table 3: PSNR and SSIM progression across implementation stages. The final two rows compare both synthetic noise variants under otherwise identical conditions.

Stage	Approach	PSNR (dB)	SSIM
Baseline	Noisy input	1.95	—
Attempt 1	Log-domain, default settings	9.99	0.5589
Attempt 2	Log-domain, clamping fixes	10.94	0.5113
Attempt 3	Pixel-Shuffle Downsampling stride 4	8.27	0.2471
Attempt 4	Log-domain, optimised	13.35	0.7754
Variant A	Log-domain, fixed Gaussian ($\sigma = 0.15$)	21.39	0.8436
Variant B	Log-domain, per-image JSON Uniform (best)	21.41	0.8358

Table 4: Complete method comparison on ICF Multiplicative Uniform noise (input PSNR: 4.60 dB, input SSIM: 0.4143). NN2I refers to Noisier2Inverse [5].

Method	PSNR (dB)	SSIM	Noise assumption met?
Noisy input	4.60	0.4143	—
Noise2Self [6]	4.75	0.0177	No ($r = 0.99$, checkerboard artifacts)
BM3D log-domain [8]	4.47	0.5181	Partial (no learning)
BM3D direct [8]	4.66	0.5338	Partial (no learning)
Log-Domain NN2I, per-image JSON (ours, best)	21.41	0.8358	Yes (log-domain, self-supervised)

Figure 5 shows BM3D log-domain qualitative outputs. Despite preserving the broad circular structure, BM3D fails to recover fine detail and produces outputs visually indistinguishable from the noisy input at these noise levels.

Figure 6 shows Noise2Self outputs. Checkerboard artifacts dominate every denoised image, confirming that the J-invariant framework fails when the pixel-independence assumption is violated.

8 Discussion

8.1 Why the Log-Domain Approach Succeeds

The log-domain framework (Section 4) succeeds for two reasons. First, the log transform converts the multiplicative model to additive (Eq. 2), enabling the additive Noisier2Inverse framework [5]. Second, the stabilisation strategy (Eqs. 16–17) gracefully handles vacuum pixels without requiring strict positivity. The +19.46 dB improvement without clean training data demonstrates that the log-domain self-supervised objective provides a meaningful training signal under ICF imaging conditions.

8.2 Why Noise2Self Fails

Noise2Self’s failure (4.75 dB, SSIM 0.0177) directly results from spatial correlation ($r = 0.99$) violating the J-invariant pixel-independence assumption [6]. This confirms that noise model compatibility is the primary determinant of denoising performance on non-standard imaging data.

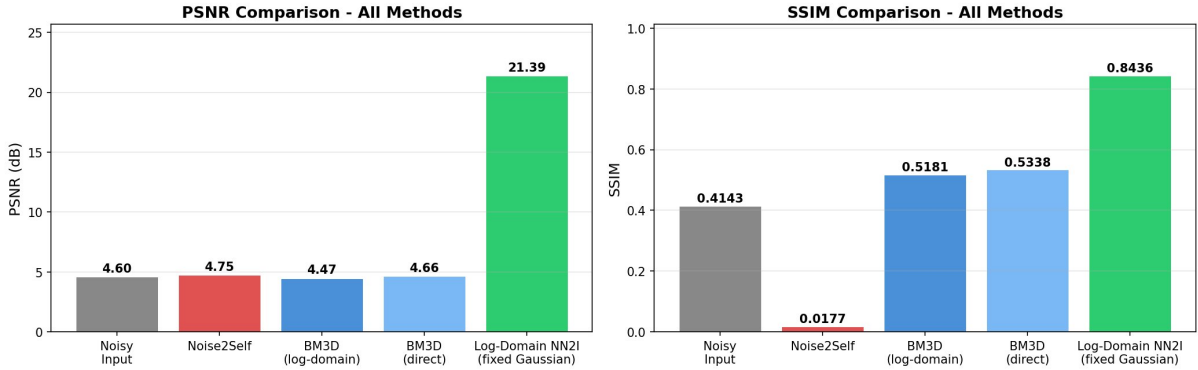


Figure 2: PSNR (left) and SSIM (right) comparison of all evaluated methods on ICF Multiplicative Uniform noise. Log-Domain Noisier2Inverse with per-image JSON noise loading (Variant B) achieves the best result: 21.41 dB PSNR and SSIM 0.8358, substantially outperforming all baselines. BM3D achieves moderate SSIM (0.52–0.53) but low PSNR (≈ 4.5 dB), consistent with over-smoothing. Noise2Self collapses to near-zero SSIM (0.0177) due to checkerboard artifacts.

8.3 Analysis of BM3D Performance

BM3D in log-domain achieves moderate SSIM (0.5181) but low PSNR (4.47 dB), marginally below the noisy input PSNR (4.60 dB). This reflects BM3D’s tendency to over-smooth: it preserves the broad circular structure (hence moderate SSIM) while losing quantitative intensity accuracy. BM3D direct (4.66 dB, SSIM 0.5338) performs marginally better, suggesting that for the spatially correlated Multiplicative Uniform noise in ICF images, the log-domain transformation alone does not provide the expected benefit for a filter-based method without learned structure.

8.4 Applicability to Experimental Images

A natural question raised by this work is whether the framework trained on synthetic ICF images generalises to real experimental data. Running an experimental image through the trained network — without retraining — would provide a direct indication of transferability and practical utility for operational ICF diagnostics at NIF. The synthetic generation pipeline (Section 5.1.1) closely follows the physical forward model of the GXD detector, suggesting the domain gap may be small; however, real experimental images may contain additional noise sources, detector artefacts, or intensity distributions not captured in the synthetic dataset. We recommend this as an immediate next step: applying the Variant A or Variant B model to an experimental GXD image and comparing the output qualitatively against available references. If the domain gap proves significant, fine-tuning on a small number of experimental images with known noise parameters (if available from detector calibration) would be a straightforward extension of the per-image JSON loading strategy already implemented in Variant B.

8.5 Remaining Error and Limitations

Two sources of residual error are identified. First, some error concentrates at the sharp vacuum–target boundary, where the steep intensity gradient is difficult for the U-Net decoder to reproduce faithfully. Second, and more significantly, the inner shell intensity gradient — the low-contrast grey region visible in the clean reference — is not fully recovered in the NN2I output, which instead produces a high-contrast binary-like reconstruction. This loss of inner shell detail is not a boundary artefact; it reflects the network collapsing the subtle intensity variation of the shell to a uniform value, likely due to the combination of log-domain training, the sigmoid output



Figure 3: Log-Domain Noisier2Inverse results — Variant A (fixed Gaussian noise, $\sigma = 0.15$). Columns (left to right): noisy input (with contrast-enhanced inset), NN2I denoised output, clean reference, difference map (yellow/white = high residual, dark = low residual). Mean PSNR: 21.39 dB, SSIM: 0.8436, input PSNR: 1.95 dB.

activation, and the low signal-to-noise ratio of the inner shell region relative to the dominant slit feature. Recovering this fine structural detail may require a loss function that explicitly weights low-contrast regions, or a perceptual loss term sensitive to local intensity gradients. Additional limitations include: evaluation against per-image ground truth obtained from collaborators rather than fully independent test data; and implicit rather than explicit handling of noise correlation.

9 Conclusion

Implementing self-supervised denoising on ICF Multiplicative Uniform noise required resolving four distinct challenges: log-domain instability at zero-valued vacuum pixels, highly correlated noise ($r = 0.99$), per-image varying parameters, and training instability.

The Log-Domain Noisier2Inverse framework (Section 4) with numerical stabilisation, per-image noise loading, and early stopping achieved a best mean PSNR of **21.41** dB and SSIM of **0.8358** (Variant B, per-image JSON Uniform noise), representing a +19.46 dB improvement over the noisy input and substantially outperforming all baselines: Noise2Self (4.75 dB, SSIM 0.0177), BM3D log-domain (4.47 dB, SSIM 0.5181), and BM3D direct (4.66 dB, SSIM 0.5338). Variant A (fixed Gaussian noise) achieves 21.39 dB PSNR and SSIM 0.8436, confirming that per-image noise matching provides a consistent benefit.



Figure 4: Log-Domain Noisier2Inverse results — Variant B (per-image JSON Uniform noise loading). Same column layout as Fig. 3. Variant B achieves the best overall result: mean PSNR 21.41 dB, SSIM 0.8358, input PSNR 1.95 dB, representing a +19.46 dB improvement over the noisy baseline.

Acknowledgements

The work of G. Hwang has been supported by the 2025 Yeungnam University Research Grant.

References

- [1] N. Naheed, B. T. Wolfe, and Z. Wang, Noise Classification of ICF Images Using a Convolutional Neural Network (CNN), *Asia Mathematika*, 7(2):27–34, 2023.
- [2] C. R. Harris, K. J. Millman, S. J. van der Walt, R. Gommers, P. Virtanen, D. Cournapeau, E. Wieser, J. Taylor, S. Berg, N. J. Smith, R. Kern, M. Picus, S. Hoyer, M. H. van Kerkwijk, M. Brett, A. Haldane, J. F. del Río, M. Wiebe, P. Peterson, P. Gérard-Marchant, K. Sheppard, T. Reddy, W. Weckesser, H. Abbasi, C. Gohlke, and T. E. Oliphant, Array programming with NumPy, *Nature*, 585:357–362, 2020. DOI: 10.1038/s41586-020-2649-2.
- [3] J. Lehtinen, J. Munkberg, J. Hasselgren, S. Laine, T. Karras, M. Aittala, and T. Aila, Noise2Noise: Learning Image Restoration without Clean Data, In *Proceedings of ICML*, 2018.
- [4] N. Moran, D. Schmidt, Y. Zhong, and P. Coady, Noisier2Noise: Learning to Denoise from Unpaired Noisy Data, In *Proceedings of the IEEE/CVF Conference on Computer Vision and Pattern Recognition (CVPR)*, pp. 12064–12072, 2020.

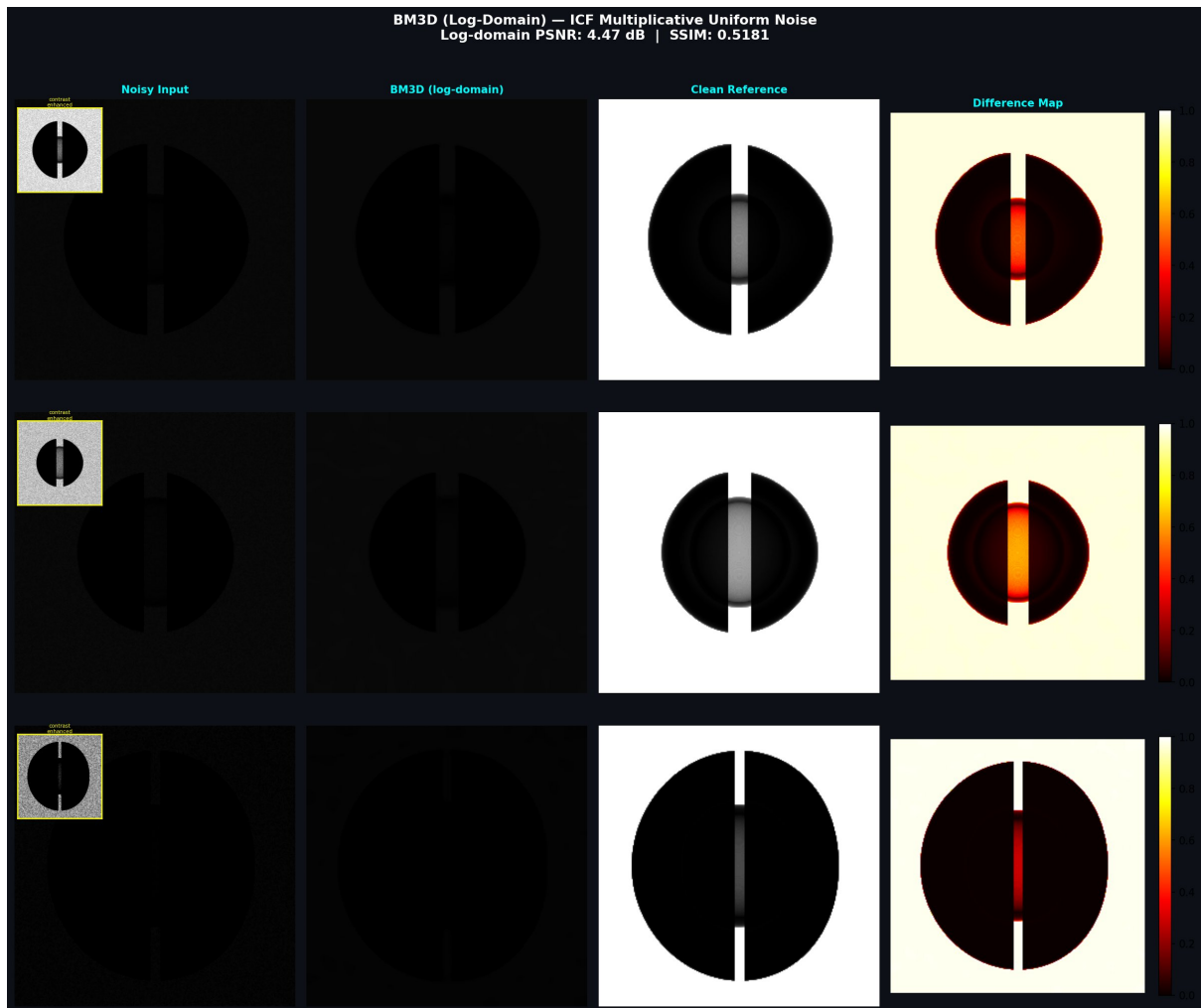


Figure 5: BM3D (log-domain) results on ICF Multiplicative Uniform noise. Columns (left to right): noisy input (with contrast-enhanced inset), BM3D log-domain denoised output, clean reference, difference map (yellow/white = high residual). Log-domain mean PSNR: 4.47 dB, SSIM: 0.5181. BM3D fails to recover meaningful structure despite moderate SSIM values.

- [5] N. Gruber, J. Schwab, M. Haltmeier, A. Biguri, C. Daska, and G. Hwang, Noisier2Inverse: Self-Supervised Learning for Image Reconstruction With Correlated Noise, *IEEE Access*, 13:139445–139459, 2025. DOI: 10.1109/ACCESS.2025.3596557.
- [6] J. Batson and L. Royer, Noise2Self: Blind Denoising by Self-Supervision, In *Proceedings of ICML*, 2019.
- [7] O. Ronneberger, P. Fischer, and T. Brox, U-Net: Convolutional Networks for Biomedical Image Segmentation, In *MICCAI*, 2015.
- [8] K. Dabov, A. Foi, V. Katkovnik, and K. Egiazarian, Image Denoising by Sparse 3-D Transform-Domain Collaborative Filtering, *IEEE Trans. Image Processing*, 16(8):2080–2095, 2007.
- [9] A. Krull, T.-O. Buchholz, and F. Jug, Noise2Void – Learning Denoising from Single Noisy Images, In *CVPR*, 2019.

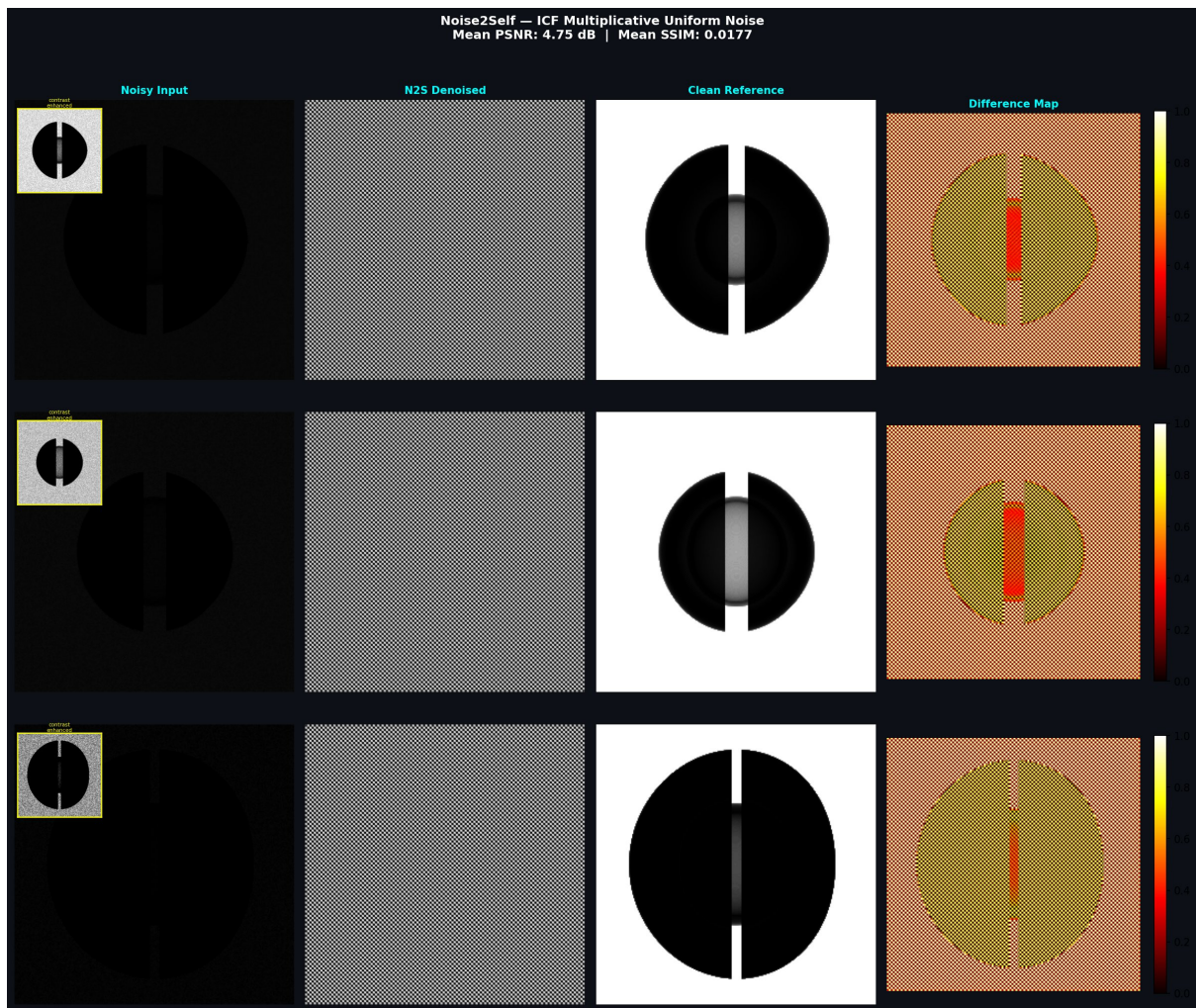


Figure 6: Noise2Self results. Columns (left to right): noisy input (with contrast-enhanced inset), N2S denoised output, clean reference, difference map (yellow/white = high residual). Checkerboard artifacts dominate the denoised output in all three examples, with no structural recovery. Mean PSNR: 4.75 dB, SSIM: 0.0177.